Research Article

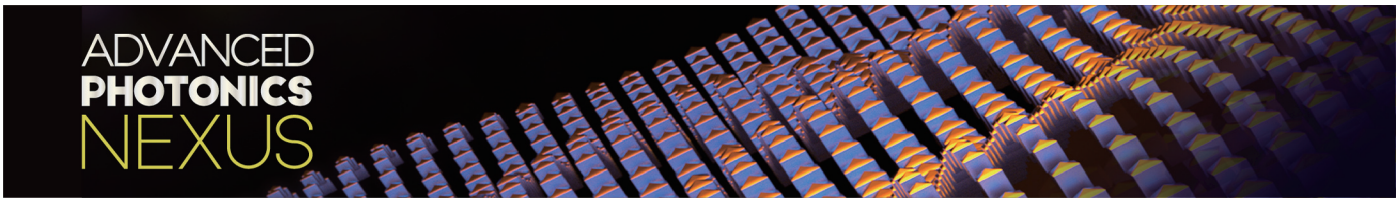

Conjugate adaptive optics extension for commercial microscopes

Alex Dorn,[a,†] Hans Zappe,[a] and Çağlar Ataman[b,*]
[a]University of Freiburg, Department of Microsystems Engineering, Laboratory for Micro-Optics, Freiburg, Germany
[b]University of Freiburg, Department of Microsystems Engineering, Microsystems for Biomedical Imaging Group, Freiburg, Germany

Abstract. We present what we believe is the first conjugate adaptive optics (AO) extension that can be retrofitted into a commercial microscope by being positioned between the camera port and the image sensor. The extension features a deformable phase plate (DPP), a refractive wavefront modulator, and indirect wavefront sensing to form a completely in-line architecture. This allows the axial position of the DPP to be optimized by maximizing an image quality metric, which is a cumbersome task with deformable mirrors as the correction element. We demonstrate the performance of the system on a Zeiss AxioVert 200M microscope equipped with a 20× 0.75 NA air objective. To simulate sample-induced complex aberrations, transparent custom-made arbitrary phase plates were introduced between the sample and the objective. We demonstrate that the extension can provide high-quality full-field correction even for large aberrations, when the DPP is placed at the conjugate plane of the phase plates. We also demonstrate that both the DPP position and its surface profile can be optimized blindly, which can pave the way for plug-and-play conjugate-AO systems.

Keywords: adaptive optics; microscopy; deformable phase plate.

Received Jun. 11, 2024; revised manuscript received Jul. 11, 2024; accepted for publication Aug. 16, 2024; published online Sep. 11, 2024.

[DOI: 10.1117/1.APN.3.5.056018]

1 Introduction

Adaptive optics (AO) is a powerful method that uses a dynamic element in the imaging and/or excitation path to actively correct for sample- and/or system-induced aberrations and restore the native performance of the instrument. In its most common form, an AO system uses a deformable mirror (DM) at the exit pupil of the imaging system, where light from all field points overlaps. This method, known as pupil-AO, can correct for field-independent aberrations, such as spherical aberration originating from refractive-index-mismatched media,[1,2] leading to substantial image enhancement across the entire field of view (FoV). However, for more complex, inhomogeneous samples, the induced wavefront distortion can vary significantly for different field points.[3–5] In this case, the aberrations are field-dependent, and pupil-AO can only provide effective corrections within a limited portion of the FoV known as the isoplanatic patch, whose size is strongly sample-dependent.

Conjugate-AO is an alternative scheme that places one or more corrective elements at planes conjugate to the main aberrating layers of the sample for correction beyond the isoplanatic patch.[6–10] For astronomical telescopes, it was shown that N DMs located at fixed planes conjugate to specific layers of the atmosphere can enhance the correction field by $4N^2$.[6] In retinal imaging, Thaung et al. demonstrated that a dual-conjugate AO can improve the diffraction-limited FoV of a fundus camera from 1.5 deg to 6.5 deg.[11] The Bifano group from Boston University has applied this method to life-science microscopy, demonstrating that a single-conjugate AO (SCAO) system can correct sample-induced and strongly field-dependent aberrations beyond the isoplanatic patch in a wide-field microscope.[12–14] When aberrations predominantly originate from a single plane, SCAO can even lead to almost full-field correction.[15,16] To address both field-dependent and independent aberrations, several groups have employed MCAO systems with two correction elements located in pupil and sample conjugate planes, respectively.[17,18]

*Address all correspondence to Çağlar Ataman, caglar.ataman@imtek.uni-freiburg.de

†Currently with SICK AG, Freiburg, Germany

Conjugate-AO with reflective corrective elements (e.g., DMs and most liquid crystal spatial light modulators) requires additional telescopic optics and folding of the beam path. The system architecture becomes prohibitively complex, as the number of correction elements increases as well. While being acceptable for astronomical applications, this complexity is a major impediment for conjugate-AO in life-science microscopy. Furthermore, as aberrations in typical biological samples arise from random planes,[9] the corrective elements should be moved along the optical axis to find their optimal location, which requires moving the entire optical arrangement.[19] Thus, conjugate-AO implementations were strictly limited to research microscopes until now. The past decade has seen the emergence of several novel refractive wavefront modulator technologies based on either piezoelectric[20,21] or electrostatic actuators,[22,23] which are functionally equivalent to DMs. Since these work in transmission, they drastically simplify pupil or conjugate-AO microscopy implementations.

In this work, we discuss the design and performance of the first conjugate-AO extension for a commercial microscope combining a refractive wavefront modulator [a Delta 7 deformable phase plate (DPP) from Phaseform GmbH] and indirect wavefront sensing.[24] The DPP is capable of replicating complex wavefront profiles in open-loop control and can reproduce Zernike modes up to the seventh radial order over a clear aperture of 10 mm.[25] It is accommodated within a simple relay optics that interfaces to the camera port of a Zeiss AxioVert 200M inverted microscope equipped with a 20× 0.75 NA air objective. Using a translation stage allowing fine position adjustment, the DPP can be displaced along the optical axis to match the conjugate plane of the aberration source. To introduce complex yet controlled aberrations that mimic sample-induced aberrations over a large FoV, we used a transparent custom-made phase screen between the sample and the objective. The induced aberrations are estimated by a modal decomposition algorithm that optimizes the power spectrum density (PSD) of the acquired images.[26] We demonstrate that at the correct conjugate plane, the scheme provides full-field correction, only limited by the aperture of the DPP. Furthermore, we also show that the optimal conjugate location of the DPP can be found by maximizing an image quality metric as a function of the axial position of the DPP.

2 Materials and Methods

2.1 Experimental Setup

Figure 1(a) shows a simplified schematic of the full-field epifluorescence inverted microscope equipped with the conjugate-AO extension featuring a DPP. A microscope is essentially a $4f$ imaging system, where the object plane is located at the focus of the objective lens, and a camera is located at its conjugate plane (e.g., the image plane). In certain imaging scenarios, aberrations can originate predominantly from a thin, axially finite region of high turbidity. Such a layer may be a nonplanar interface between different biological areas with different refractive indices, such as the cornea of the human eye in retinal imaging[27] or the intact rodent skull in transcranial neural imaging.[28,29] In this case, the aberrating layer can be simply modeled as a two-dimensional refractive layer, which modulates the phase of the propagating light field. In this model, the layer is infinitesimally thin and is located at a distance d from the object plane within the working distance of the objective. In conjugate-AO, the correction device is located at a plane conjugate to this aberration plane, indicated as $d' = dM^2$ in Fig. 1(a), where M is the magnification of the objective (20× in this case). When the spatial phase modulation matches the inverse of the aberrating layer, the induced phase modulation is compensated for all fields simultaneously, resulting in a correction over the entire FoV, given that the corrective element has sufficient aperture size. Otherwise, a light cone, originating from the point at the periphery of the FoV, experiences vignetting caused by the restricted clear aperture of the correction element after propagation distance d'. For a clear aperture radius r_{DPP}, the maximum correctable $\mathrm{FoV}_{\mathrm{image}}$ in the image plane can be calculated as

$$\mathrm{FoV}_{\mathrm{image}} = r_{\mathrm{DPP}} - d'\mathrm{NA}_{\mathrm{image}}, \tag{1}$$

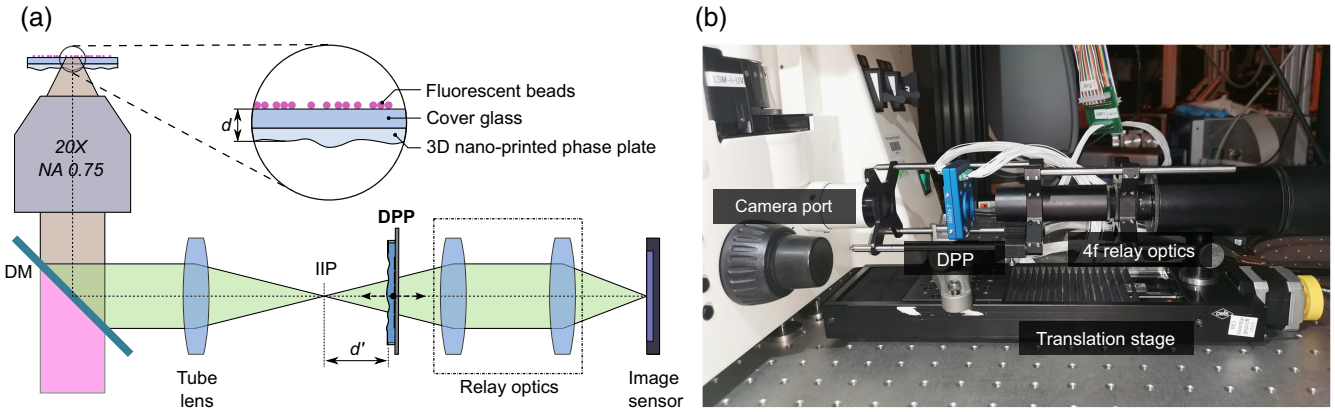

Fig. 1 The experimental setup. (a) Schematic representation of a full-field epifluorescence inverted microscope with the conjugate-AO extension. The microscope, represented by the objective, DM, and the tube lens, images the sample on the intermediate image plane (IIP), where the image sensor is normally located. To be able to position the DPP at a plane conjugate to the aberrating layer, the extension features $4f$ optics that re-images the IIP on the image sensor with minimal aberrations. The inset depicts the structure of the synthetic samples manufactured to test the performance of the AO extension. (b) Photograph of the conjugate-AO extension attached to a commercial microscope.

where NA_{image} refers to the image-side numerical aperture (NA), corresponding to the object-side NA (0.75 in this case) divided by the magnification M. With the fixed DPP radius r_{DPP} of 5 mm, the FoV correctable without vignetting decreases linearly with increasing separation distance d between the object plane and the aberrating layer. For the specific samples used in the experimental work here, the aberrating layer is separated by 170 μm from the object plane, leading to a maximal correctable image radius ($FoV_{object}/2$) of 120 μm with the DPP positioned 68 mm away from the intermediate image plane.

Figure 1(b) shows the experimental arrangement of the conjugate-AO extension developed in this work. The base microscope is a commercial inverted microscope (Zeiss AxioVert 200M) operated in the epi-illumination modality. Fluorescent beads dispersed on a cover glass are imaged through an aberrating phase plate (APP). The APP is located on the opposite side of the beads on the 170 μm thick cover glass, which sets a well-defined distance between the object's and APP's plane [Fig. 1(a)]. The intermediate image at the camera port of the microscope was relayed with a Keplerian telescope on the camera sensor. The relay optics comprised lenses RL_1 and RL_2 with focal lengths of 200 and 500 mm, respectively, providing an additional magnification of 2.5×. The DPP was placed into the imaging path between the microscope's camera port and the first lens of the relay optics on a computer-controlled translation stage (LTM 120, OWIS Gmbh, Germany).

2.1.1 Impact on imaging performance

Integrating an AO module into a microscope can influence the native performance, as the initial flatness error of the dynamic element can degrade the optical performance and should be corrected alongside any other system and/or sample-induced aberrations. Therefore, the impact of the DPP-based AO module on the microscope performance was assessed by imaging 450 nm fluorescent beads again dispersed on a 170 μm thick cover glass both with and without the AO attachment, using a green filter of $\lambda = 525$ nm center wavelength on the detection arm. A 20×/0.75 NA air objective collected the fluorescence emission. Along with an additional 2.5× magnification provided by the relay optics, the total system magnification was 50×. This additional magnification was necessary to meet the Nyquist sampling, as the sensor was a 2048 pixel × 2048 pixel camera (pco edge 4.2 bi) with individual pixels measuring 6.5 μm. With a total magnification of 50× and the sensor dimensions of 13.31 mm × 13.31 mm, the FoV size in object space was 266.2 μm × 266.2 μm.

Figure 2 shows the change in the (approximate) system point spread function (PSF), measured as the width of a single fluorescent bead, at five different points on the FoV positions with the introduction of the conjugate-AO extension at the user-perceived best focus position. The theoretical diffraction-limited FWHM value for imaging a 450 nm bead at a wavelength of $\lambda = 525$ nm with an NA of 0.75 is ≈495 nm. This value was calculated assuming a Gaussian-shaped object with an FWHM of 450 nm to represent the beads. Without the AO attachment in the imaging path, the FWHM values of the beads are on average 16% larger than the theoretical diffraction-limited values. This initial deviation from the theoretical FWHM is attributed to the introduction of additional optical components within the relay optics. With the DPP in its initial (e.g., passive) state, the spot size slightly increases due to its initial flatness error. However, when the DPP was brought to its best-flat condition, the imaging performance was significantly restored to a level similar to that without the DPP in the imaging path.

2.1.2 Sensorless aberration estimation

Due to the general lack of standard "guide stars," many AO microscopes employ indirect wavefront sensing, in which the aberrations are estimated indirectly from the camera images. Modal decomposition is a well-known technique for estimating wavefront aberrations in the imaging process without the use of a wavefront sensor.[26,30–32] This approach involves estimating the individual contributions of a set of orthogonal basis aberration modes (i.e., Zernike modes) separately. The improvement in the image quality is monitored via a specific metric (i.e., signal intensity, width of the modulation transfer function, etc.). In this work, we exclusively utilized the PSD as the quality metric. It is assumed that a PSD of a high-quality image encompasses high-frequency elements that correspond to sharp-edge transitions, while a low-quality image contains primarily low-frequency components near DC. Therefore, the integral sum of the PSD within a specific spatial frequency range can provide a quantitative measure of image quality. In this work, the integration range is chosen to be from 5% to 25% of the maximum frequency range supported by image plane sampling. Frequencies below and above this range are excluded in order to reject DC components and high-frequency noise, respectively.

Figure 3(a) shows the procedure for estimating the mode amplitude for a single Zernike mode (Z_3^1) with fluorescent beads as a sample. The main assumption is that the image quality metric is a convex function with a Gaussian profile of any mode amplitude and remains orthogonal to other modes. Consequently, if the image quality metric is recorded as a function of known aberration mode amplitudes at three bias points, the relative contribution of this particular mode can be estimated as the coefficient for which the metric function is maximized. This process is repeated for the n modes that are considered for correction. Given that the conjugate-AO scheme is anticipated to provide full-field correction with the specific type of synthetic sample in use, the quality metric calculations were conducted over the largest rectangular portion of the imaged FoV, which was not obstructed by the DPP.

2.2 Manufacturing of Test Samples

In order to be able to correlate the estimated wavefront aberrations with ground truth, we manufactured dedicated test samples comprising a nominally 170 μm thick microscope slide with dispersed fluorescent beads on one side, and a 3D nanoprinted APP on the other. The APPs were fabricated using a two-photon polymerization 3D printer (Nanoscribe Photonics Professional GT+) and characterized using a white-light interferometer (Zygo NewView 9000). The photopolymer had a refractive index of $n_d = 1.62$ at the d-line after polymerization. We have prepared two different APPs with different aberration profiles and amplitudes. The one with an OPD of 0.64 μm: RMS is hereafter referred to as the APP1 and the APP with an OPD of 1.26 μm: RMS to as the APP2. Both OPD values refer to the full aperture of the APPs with a radius of 250 μm.

3 Results

3.1 Conjugate Correction

The conjugate-AO experiments were performed on a commercial inverted full-field microscope (Zeiss AxioVert 200M) in

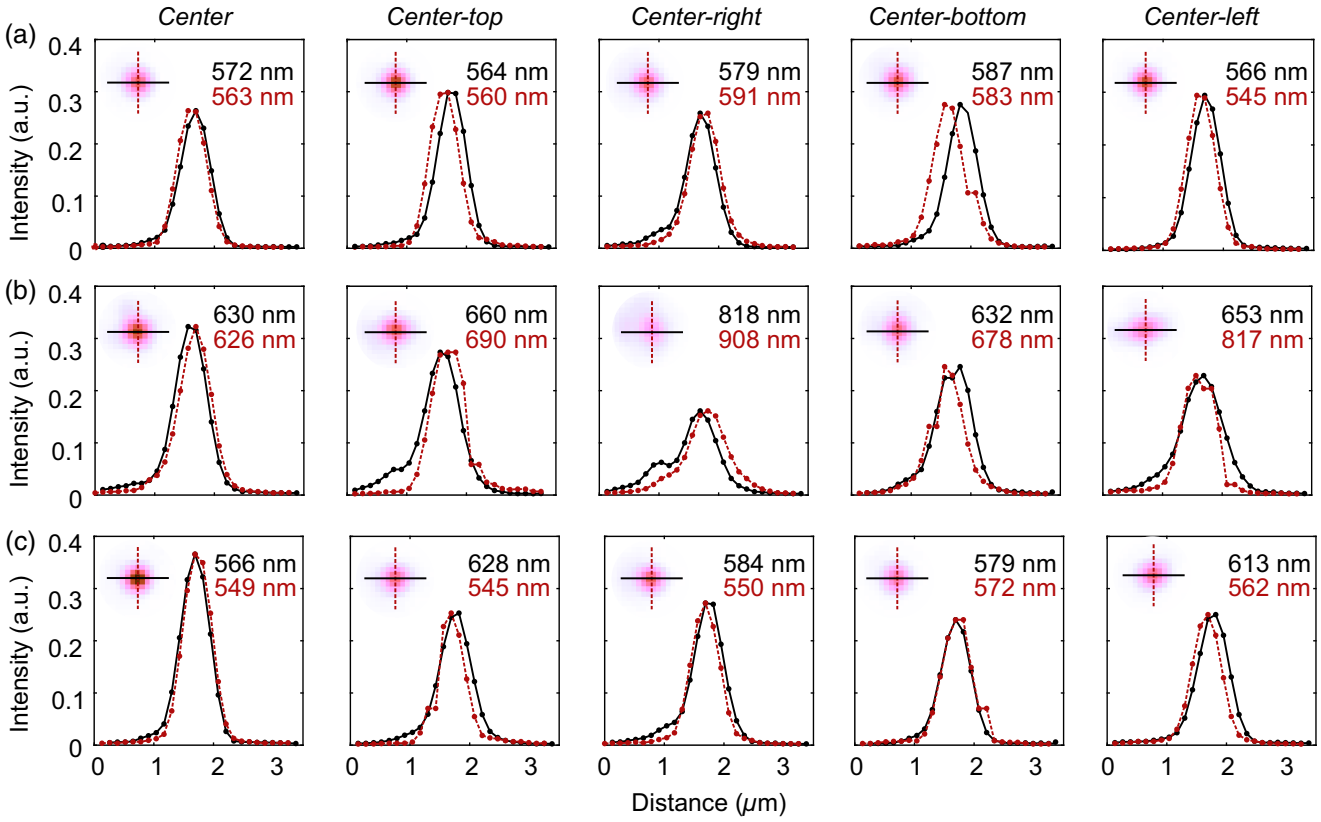

Fig. 2 Impact of the conjugate-AO extension on the native imaging performance of the microscope. (a) Approximate PSF of the microscope at five different points on the FoV in the absence of the DPP within the AO extension in the imaging path. The insets on the left in each figure depict the spot images, plotted in negative color for clarity. The respective location of each PSF within the FoV is indicated by the column labels. The FWHM spot size of each PSF along the x– and y–axes are indicated on the plots as well. (b) The same plots with the AO attachment and the DPP at its initial state. The initial flatness error of the DPP leads to a slight increase in the PSF widths. (c) The DPP is actively brought to the best-flat state.

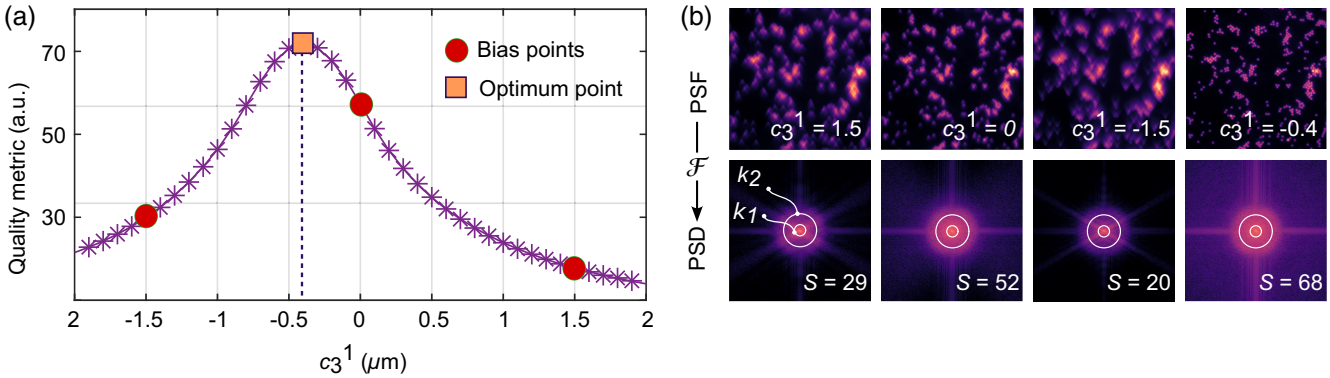

Fig. 3 Estimation of the aberration mode amplitudes for the modal decomposition algorithm, demonstrated for the Zernike mode Z_3^1. (a) The image quality metric as a function of the mode amplitude coefficient, which is a convex function whose maximum corresponds to the contribution of this specific mode. (b) Calculation of the image quality metric based on the integration of the PSD within a spatial frequency range of k_1 and k_2. To minimize the measurement time, this metric is calculated at different bias points ($c_3^1 = -0.4, -1.5, 0, 1.5$), and the results are fitted to a Gaussian curve. The mode coefficient corresponding to the maximum of this curve is chosen as the amplitude of that mode.

epifluorescence mode, equipped with a $20\times/0.75$ NA air immersion objective. For each test sample, the axial position of the DPP was first adjusted to be approximately conjugate to the APP using the motorized z-stage. A region of interest (RoI) of $230\ \mu m \times 230\ \mu m$ was selected for correction, as this size closely matched the dimensions of the largest FoV that could be corrected without vignetting with the DPP in this specific location. To minimize the fluorescence background, the illumination field aperture was adjusted accordingly. The modal decomposition algorithm described above was used for aberration estimation, with an initial bias interval of $[-1.2\ \mu m, 1.2\ \mu m]$ for all modes. All Zernike modes up to the fourth radial order, excluding piston, tip, and tilt, corresponding to a total of 12 modes used in the correction. The algorithm was run in five iterations, where in each iteration the bias interval was reduced by $0.2\ \mu m$. The process used 180 images in total with a runtime of 65 s, limited primarily by the speed of the image acquisition software.

The comparison of sample images before and after correction for APP1 is shown in Fig. 4(a). The uncorrected image was recorded at the user-perceived best focus position with the DPP in its best-flat condition. After correction, the image quality significantly improved all across the image. As the enlarged views of the insets in Fig. 4(b) indicate, only at the periphery

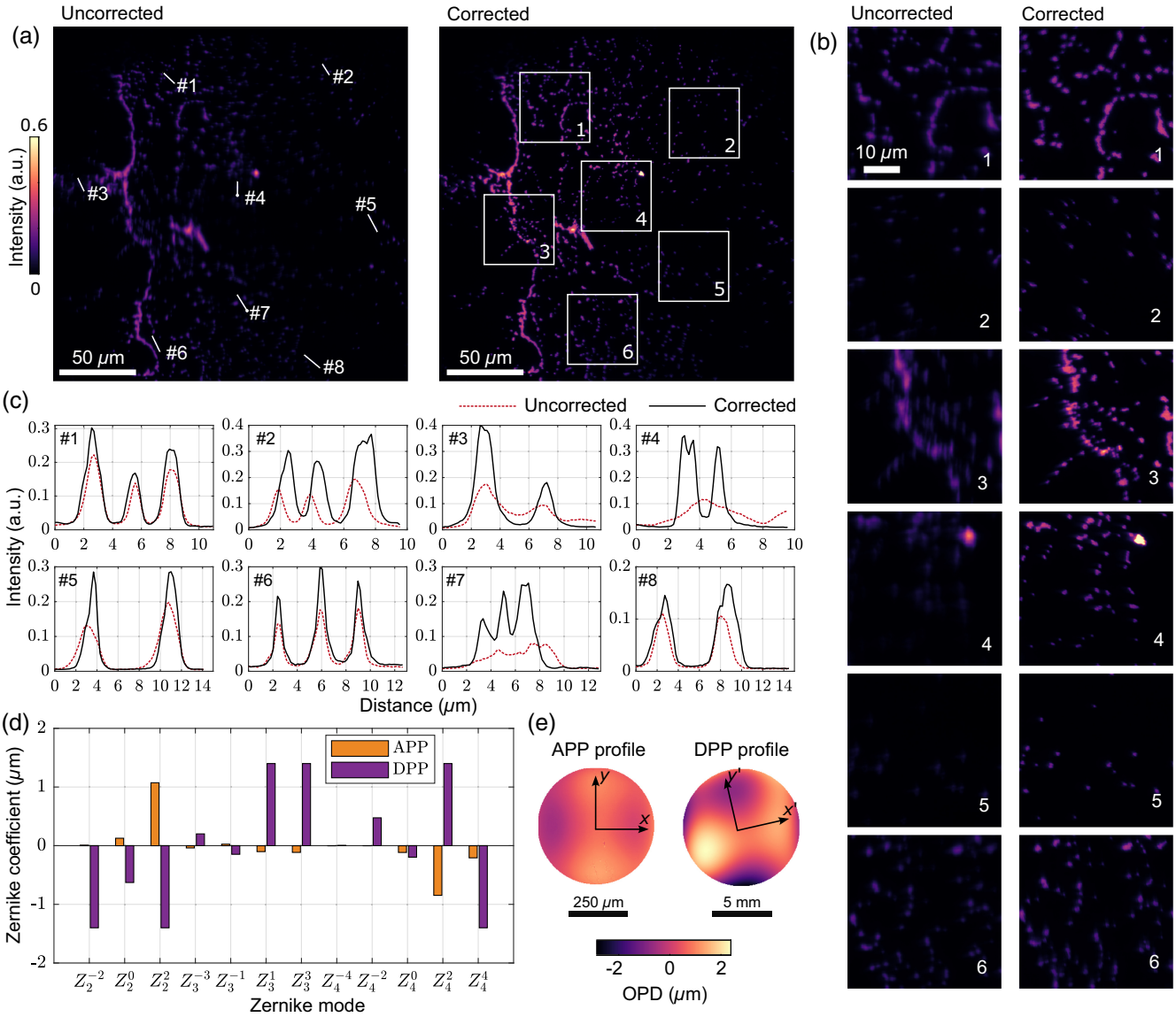

Fig. 4 Correction performance of the conjugate-AO extension with APP1 as the sample. (a) Uncorrected (left) and corrected (right) images of the beads. The cross-sectional intensity profiles along the eight lines are indicated on the uncorrected image. (b) Close-up view of the six square areas within the FoV indicated on the corrected image. (c) The cross-sectional intensity profiles along the eight lines are indicated on the uncorrected image. (d) Measured APP1 profile (orange), and the DPP correction profile calculated using the open-loop model and the drive signals (purple). (e) Zernike decomposition of both profiles indicating a significant qualitative difference between the ground truth and the estimated profiles.

of the RoI, the correction quality begins to deteriorate due to vignetting. A more quantitative assessment of the correction performance follows from the cross-sectional plots at eight different locations shown in Fig. 4(c) (left). Due to the complex aberration profile, the uncorrected image indicates strong field-dependent aberrations. For the cross section #1, for instance, the beads can be resolved with almost diffraction-limited resolution. On the other hand, the cross sections #3 and #7 show a complete loss of resolution due to the aberrating layer. The conjugate-AO scheme could recover near diffraction-limited resolution across the entire RoI, indicating that the DPP could effectively compensate for the APP1. Figure 4(d) shows the fitted Zernike coefficients of modes up to the fourth radial order corresponding to the APP1 and the calculated open-loop DPP profile after correction, with both profiles plotted in Fig. 4(e). The estimated profile qualitatively matches that of the APP1 profile apart from a rotation angle. The open-loop DPP control algorithm assumes a linear relationship between the control signal and the deformation. However, at large strokes, the response deviates from linearity,[22,23] leading to an amplitude difference between the intended and replicated profiles.

Figure 5 summarizes the correction performance with APP2 as the sample. Due to the stronger aberration profile, the uncorrected image has almost no discernible beads. Despite this poor

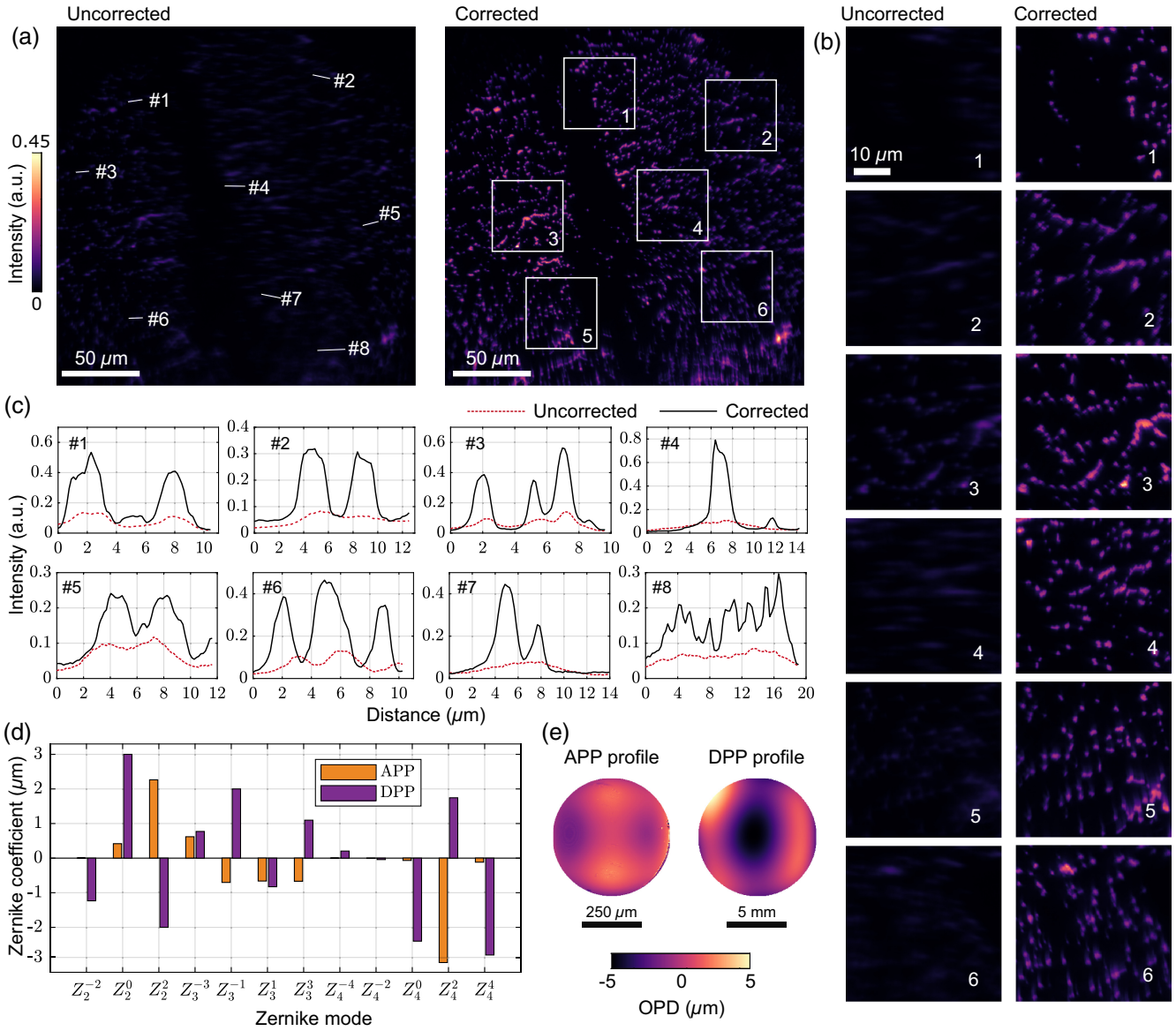

Fig. 5 Correction performance of the conjugate-AO extension with APP2 as the sample. (a) Uncorrected (left) and corrected (right) images of the beads. The cross-sectional intensity profiles along the eight lines indicated on the uncorrected image. (b) Close-up view of the six square areas within the FoV indicated on the corrected image. (c) The cross-sectional intensity profiles along the eight lines indicated on the uncorrected image. (d) Measured APP2 profile (orange), and the DPP correction profile calculated using the open-loop model and the drive signals (purple). (e) Zernike decomposition of both profiles indicating a significant qualitative difference between the ground truth and the estimated profiles.

initial image quality, the conjugate-AO scheme could again substantially improve the image quality. The overall correction quality across the entire FoV, however, is not as consistent compared to that of Figs. 4(a) and 4(b), indicating residual aberrations. The size of the imaged beams is also consistently larger than the diffraction limit. In particular, the bottom-right corner of the image has clear residual field-dependent aberrations, which can also be deduced from Fig. 5(e), with the estimated aberration profile deviating significantly from the ground truth. This is due to the profile of APP2 being beyond the stroke range of the DPP. As a result, the DPP can only provide a partial correction. The open-loop control scheme that we use to drive the DPP is based on constrained optimization. We have previously shown that when the aberration profile is beyond the capabilities of the DPP, the control software is still capable of converging to a solution that is optimal within the available space of possible drive signals.[33] A DPP with higher stroke would be capable of improving the residual aberrations without adversely affecting the correction quality of other areas.

3.2 Optimization of the DPP Position

For all the imaging experiments discussed until now, the DPP was located at a plane calculated to be conjugate to the aberration layers in the samples. While this is useful to illustrate the power of conjugate-AO for samples of similar type, its real-life potential is limited due to the simple fact that with most sample types, the location of the aberrating layer with respect to the focal plane, and thus the optimum location for the corrective element is unknown. Featuring a refractive correction element and sensorless aberration estimation, the conjugate-AO extension enables the optimization of not only the DPP profile but also its axial/conjugate position. Figure 6 shows the maximum image quality metric attainable by the conjugate correction at different DPP positions for both APPs. It should be noted that a separate correction is performed at each DPP location, without any assumption about the location of the aberrating layer.

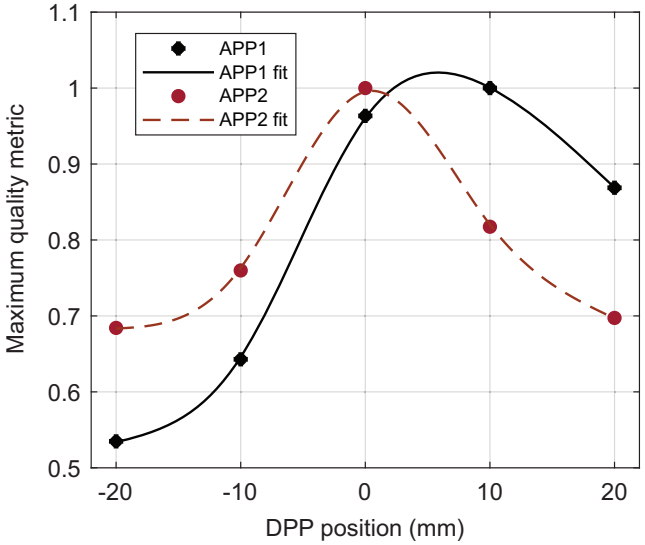

Fig. 6 Maximum image quality metric as a function of correction plane location with a new correction routine run at every data point. The DPP position on the *x* axis refers to the distance from the intermediate image plane.

For both APPs, the curves show a clear maximum, which is within the vicinity of the calculated position of the optimal correction plane located 125 μm right to the intermediate image plane. The small difference in the optimal positions for the two APPs can be attributed to the variation in the thickness of the microscope slides, the difference in the thicknesses of the two APPs, and the low sensitivity of the image quality metric to the position of the DPP.

4 Discussion

In this work, we used an inverted wide-field epifluorescence microscope with flood illumination, and the AO module was placed only in the imaging path. The sensorless aberration estimation method uses the PSD of the recorded images as a quality metric. Due to the lack of axial sectioning capability of the microscope, both in-focus and out-of-focus lights contribute to image formation. This significantly reduces the contrast of the recorded images, and renders monitoring of small changes in the image PSD difficult, resulting in inaccurate image-based aberration estimation. Therefore, this particular microscope is not suitable for imaging complex 3D biological specimens, for which the conjugate-AO scheme would be most beneficial. The synthetic samples used in this work had beads in a single plane, mimicking the images from an axial scanning microscope, and making it possible to demonstrate the performance of the AO module with a wide-field microscope.

For different microscopy methods with axial scanning capability, aberrations can play a major role in both the excitation and imaging paths. For example, in a confocal microscope, both the excitation and collection paths require aberration correction, as resolution and contrast are directly correlated to the excitation and collection spot profiles. A module placed between the confocal scanning unit and the microscope's camera port can correct both the excitation and collection spot profiles. In light-sheet microscopy, the excitation and imaging paths are completely decoupled. On the imaging arm, this AO module can be used in the same way as demonstrated in this work.

5 Conclusion

We discussed the implementation of the first conjugate-AO extension for commercial microscopes and documented its performance in correcting for aberrations predominantly originating from a single layer within the sample. Featuring a refractive modulator in the form of a DPP and indirect aberration sensing, the extension is completely in-line and can be simply inserted between the camera port and the image sensor. This architecture allows straightforward translation of DPP along the optical axis, thus finding the optimum location for conjugate-AO correction. Imaging experiments using custom-developed samples indicate that when not limited by the stroke of the DPP, the extension is capable of high-fidelity, full-field correction limited by the native performance of the instrument. For larger aberrations, the extension still provides substantial image quality improvement, but cannot reach the diffraction limit, predominantly due to the stroke limitation of the DPP.

Disclosures

C.A. and H.Z. declare commercial interest in the company Phaseform GmbH, Freiburg, Germany.

Code and Data Availability

The data that support the findings of this study are available from the corresponding author upon reasonable request.

Acknowledgments

The authors would like to thank Dr. Roland Nitschke from the Life Imaging Center, Freiburg, Germany, for the provided microscopic equipment and useful discussions.

References

1. M. J. Booth, M. A. Neil, and T. Wilson, "Aberration correction for confocal imaging in refractive-index-mismatched media," *J. Microsc.* **192**(2), 90–98 (1998).
2. J. Cui et al., "Generalised adaptive optics method for high-NA aberration-free refocusing in refractive-index-mismatched media," *Opt. Express* **30**(7), 11809–11824 (2022).
3. M. Schwertner et al., "Measurement of specimen-induced aberrations of biological samples using phase stepping interferometry," *J. Microsc.* **213**(1), 11–19 (2004).
4. M. Schwertner, M. J. Booth, and T. Wilson, "Characterizing specimen induced aberrations for high NA adaptive optical microscopy," *Opt. Express* **12**(26), 6540–6552 (2004).
5. D. L. Fried, "Anisoplanatism in adaptive optics," *J. Opt. Soc. Am.* **72**, 52–61 (1982).
6. J. M. Beckers, "Increasing the size of the isoplanatic patch with multiconjugate adaptive optics," in *Very Large Telesc. and Their Instrum.*, Vol. **2**, p. 693 (1988).
7. D. C. Johnston and B. M. Welsh, "Analysis of multiconjugate adaptive optics," *J. Opt. Soc. Amer. A* **11**, 394–408 (1994).
8. F. J. Rigaut, B. L. Ellerbroek, and R. Flicker, "Principles, limitations, and performance of multiconjugate adaptive optics," *Proc. SPIE* **4007**, 1022–1031 (2000).
9. R. D. Simmonds and M. J. Booth, "Modelling of multi-conjugate adaptive optics for spatially variant aberrations in microscopy," *J. Opt.* **15**, 094010 (2013).
10. F. Rigaut and B. Neichel, "Multiconjugate adaptive optics for astronomy," *Annu. Rev. Astron. Astrophys.* **56**, 277–314 (2018).
11. J. Thaung et al., "Dual-conjugate adaptive optics for wide-field high-resolution retinal imaging," *Opt. Express* **17**, 4454–4467 (2009).
12. J. Mertz, H. Paudel, and T. G. Bifano, "Field of view advantage of conjugate adaptive optics in microscopy applications," *Appl. Opt.* **54**, 3498–3506 (2015).
13. J. Li et al., "Conjugate adaptive optics in widefield microscopy with an extended-source wavefront sensor," *Optica* **2**, 682–688 (2015).
14. J. Li, T. G. Bifano, and J. Mertz, "Widefield fluorescence microscopy with sensor-based conjugate adaptive optics using oblique back illumination," *J. Biomed. Opt.* **21**, 121504 (2016).
15. Y. Kwon et al., "Computational conjugate adaptive optics microscopy for longitudinal can lead of cortical myelin," *Nat. Commun.* **14**, 105 (2023).
16. Q. Zhao et al., "Large field of view correction by using conjugate adaptive optics with multiple guide stars," *J. Biophotonics* **12**(2), e201800225 (2019).
17. D. Gong and N. F. Scherer, "Tandem aberration correction optics (TACO) in wide-field structured illumination microscopy," *Biomed. Opt. Express* **14**, 6381–6396 (2023).
18. K. M. Hampson et al., "Closed-loop multiconjugate adaptive optics for microscopy," *Proc. SPIE* **11248**, 1124809 (2020).
19. H. P. Paudel et al., "Axial range of conjugate adaptive optics in two-photon microscopy," *Opt. Express* **23**, 20849–20857 (2015).
20. S. Bonora et al., "Wavefront correction and high-resolution *in vivo* OCT imaging with an objective integrated multi-actuator adaptive lens," *Opt. Express* **23**(17), 21931–21941 (2015).
21. H. G. Gowda, U. Wallrabe, and M. C. Wapler, "Higher order wavefront correction and axial scanning in a single fast and compact piezo-driven adaptive lens," *Opt. Express* **31**(14), 23393–23405 (2023).
22. K. Banerjee et al., "Optofluidic adaptive optics," *Appl. Opt.* **57**(22), 6338–6344 (2018).
23. P. Rajaeipour et al., "Cascading optofluidic phase modulators for performance enhancement in refractive adaptive optics," *Adv. Photonics* **2**(6), 066005 (2020).
24. A. Dorn et al., "Flexible conjugate adaptive optics with a refractive wavefront modulator," *Proc. SPIE* **11966**, 1196607 (2022).
25. P. Rajaeipour et al., "Seventh-order wavefront modulation with a gravity-neutral optofluidic deformable phase plate," *J. Opt. Microsyst.* **1**(3), 034502 (2021).
26. D. Débarre, M. J. Booth, and T. Wilson, "Image based adaptive optics through optimisation of low spatial frequencies," *Opt. Express* **15**(13), 8176–8190 (2007).
27. Y. Zhou et al., "Characterizing refractive index and thickness of biological tissues using combined multiphoton microscopy and optical coherence tomography," *Biomed. Opt. Express* **4**(1), 38–50 (2013).
28. J.-H. Park, W. Sun, and M. Cui, "High-resolution *in vivo* imaging of mouse brain through the intact skull," *Proc. Natl. Acad. Sci. U. S. A.* **112**(30), 9236–9241 (2015).
29. Z. Qin et al., "Deep tissue multi-photon imaging using adaptive optics with direct focus sensing and shaping," *Nat. Biotechnol.* **40**(11), 1663–1671 (2022).
30. M. J. Booth et al., "Adaptive aberration correction in a confocal microscope," *Proc. Natl. Acad. Sci. U. S. A.* **99**(9), 5788–5792 (2002).
31. D. Débarre et al., "Image-based adaptive optics for two-photon microscopy," *Opt. Lett.* **34**(16), 2495–2497 (2009).
32. M. Žurauskas et al., "Isosense: frequency enhanced sensorless adaptive optics through structured illumination," *Optica* **6**(3), 370–379 (2019).
33. P. Rajaeipour et al., "Optimization-based real-time open-loop control of an optofluidic refractive phase modulator," *Appl. Opt.* **58**(4), 1064–1072 (2019).

Alex Dorn received his bachelor's, master's degrees, and PhD from the University of Freiburg, Freiburg, Germany, in 2017, 2019, and 2024, respectively. He is currently a development engineer at Sick AG, Waldkirch, Germany.

Hans Zappe received his bachelor's and master's degrees from MIT, Cambridge, Massachusetts, USA, in 1983, and his PhD from the University of California at Berkeley, Berkeley, California, USA, in 1989, all in electrical engineering. He has worked at IBM, Essex, Vermont, USA, the Fraunhofer Institute for Applied Solid State Physics, Freiburg, Germany, and the Centre Suisse d'Electronique et de Microtechnique, Switzerland. He joined the Department of Microsystems Engineering, University of Freiburg, Freiburg, Germany, in 2000.

Çağlar Ataman received his PhD in electrical engineering from the Koç University, Istanbul, Turkey, in 2008, and worked as a postdoctoral researcher at the École Polytechnique Fédérale de Lausanne, in Switzerland, between 2008 and 2012. From 2012 to 2021, he was a senior scientist at the Department of Microsystems Engineering of the University of Freiburg, Germany, where he has been an assistant professor since 2021, leading the Microsystems for Biomedical Imaging Group.